The Influence of Hydrogenation and Oxygen Vacancies on Molybdenum Oxides Work Function and Gap States for Application in Organic Optoelectronics

Maria Vasilopoulou,[*,†] Antonios M. Douvas,[†] Dimitra G. Georgiadou,[†] Leonidas C. Palilis,[‡] Stella Kennou,[§] Labrini Sygellou,[§] Anastasia Soultati,[†] Ioannis Kostis,[†,‖] Giorgos Papadimitropoulos,[†] Dimitris Davazoglou,[†] and Panagiotis Argitis[†]

[†]Institute of Microelectronics, NCSR Demokritos, Terma Patriarchou Grigoriou, 15310 Aghia Paraskevi, Greece
[‡]Department of Physics, University of Patras, 26500 Patras, Greece
[§]Department of Chemical Engineering, University of Patras, 26500 Patras, Greece
[‖]Department of Electronics, Technological and Educational Institute of Pireaus, 12244 Aegaleo, Greece

Ⓢ *Supporting Information*

ABSTRACT: Molybdenum oxide is used as a low-resistance anode interfacial layer in applications such as organic light emitting diodes and organic photovoltaics. However, little is known about the correlation between its stoichiometry and electronic properties, such as work function and occupied gap states. In addition, despite the fact that the knowledge of the exact oxide stoichiometry is of paramount importance, few studies have appeared in the literature discussing how this stoichiometry can be controlled to permit the desirable modification of the oxide's electronic structure. This work aims to investigate the beneficial role of hydrogenation (the incorporation of hydrogen within the oxide lattice) versus oxygen vacancy formation in tuning the electronic structure of molybdenum oxides while maintaining their high work function. A large improvement in the operational characteristics of both polymer light emitting devices and bulk heterojunction solar cells incorporating hydrogenated Mo oxides as hole injection/extraction layers was achieved as a result of favorable energy level alignment at the metal oxide/organic interface and enhanced charge transport through the formation of a large density of gap states near the Fermi level.
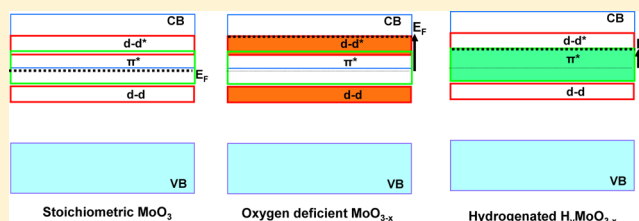
INTRODUCTION

Optoelectronic devices based on organic semiconductors (OSCs), such as organic light-emitting diodes (OLEDs)[1−4] and organic photovoltaics (OPVs),[5−7] can exhibit the remarkable combination of low-cost fabrication, flexibility and exceptional performance characteristics. In these devices, electrode interfacial layers are usually utilized to facilitate charge injection into (or charge extraction from) the OSC layers.[8,9] Transition metal oxides (TMOs) have been recognized as one of the most promising class of materials that are widely used as anode/cathode interfacial layers to enhance charge exchange with organic molecules.[10−36] Molybdenum trioxide (MoO_3) in particular has drawn considerable attention,[19−36] due to the significant improvement that it induces in the performance of OLEDs and OPVs, which is primarily attributed to the decrease of the hole injection/extraction barrier at the anode/organic interfaces. The low charge injection/extraction barriers at MoO_3/OSCs interfaces are believed to be a result of favorable energy level alignment between the MoO_3 and organic semiconducting molecules.[37] This is a result of the oxide's deep electronic energy levels and high work function value that allow facile charge transfer to/

from the highest occupied molecular orbital (HOMO) of an organic molecule. Indeed, it was recently demonstrated that favorable energy-level alignment at the metal oxide/organic interface occurs when the oxide work function is larger than the ionization energy of the organic material.[38] On the other hand, substoichiometric molybdenum oxides (MoO_x, $x < 3$), formed mainly by thermal evaporation, were recently used to enhance hole exchange in OLEDs[31−33] and OPVs,[34−36] due to their improved n-type conductivity originated from intrinsic oxygen vacancies.[38] However, a large increase in the density of oxygen vacancies may disrupt the oxides' favorable energy-level alignment with an organic semiconductor as a result of the decrease of the oxide work function.[39]

We have recently investigated the electronic structures of representative TMOs, such as tungsten and molybdenum oxide films. Deposition in reducing environments resulted in the formation of oxygen-deficient (termed also as substoichiometric) metal oxide films that were used for organic optoelectronic device applications.[40−43] Motivated by various

studies according to which hydrogen can act as a shallow donor in several metal oxides (e.g., ZnO, VO_2),[44−46] in this work we use a simple, cost-effective method to prepare hydrogenated Mo oxides and to clarify the beneficial role of hydrogenation in tuning the electronic structure (i.e work function, position of gap states) of Mo oxides for applications in organic optoelectronic devices. We present evidence that both oxygen deficiency and hydrogenation result in occupation of large density of states lying within the forbidden gap, deeper for the former (d−d bands attributed to metal−metal bond formation) and shallower for the latter (π^* band near the Fermi level). Upon a certain degree of oxygen deficiency, occupation of the antibonding d−d* band, located above the π^* and within the conduction band, results in a shift of the Fermi level toward higher energies and a corresponding decrease in the oxide work function. On the other hand, hydrogen reduction is advantageous for these oxides as they maintain nearly the same high work function for high degrees of reduction, whereas they exhibit a high density of occupied gap states near the Fermi level. These key characteristics, namely, high work function and occupied gap states near the E_F, are critical for the optimal operation of organic optoelectronic devices. Upon the implementation of hydrogenated Mo oxides as hole injection/extraction (anode interfacial) layers in F8BT-based OLEDs and P3HT:PCBM-71 bulk heterojunction OPVs, improved device performance was achieved, compared to devices with either stoichiometric MoO_3 or oxygen-deficient Mo oxide with equal work function, respectively. These findings demonstrate the tremendous potential of hydrogenation of Mo oxides, which creates an advanced class of TMO-based functional materials with tailored electronic and physical properties, and may pave the way for finding new oxide formulations that can be used not only as highly efficient charge exchange/electrode modification layers in a wide range of optoelectronic/photonic devices, but also in other diverse applications such as in photocatalysis and fuel cells.[47,48]

■ EXPERIMENTAL SECTION

Molybdenum Oxide Films Preparation. Stoichiometric MoO_3, oxygen-deficient (reduced in nitrogen environment) $MoO_{3−x1}$ and hydrogenated $H_yMoO_{3−x}$ films, were deposited in a homemade system, consisting of a stainless steel reactor, similar to the one previously presented.[49,50] The sample was positioned on an aluminum susceptor, 2.5 cm below a Mo filament heated by an (AC) current flowing through two Cu leads. The new system[51] also includes two fast responding valves, similar to those used for atomic layer deposition (ALD), through which small amounts of gases may be metered into the reactor producing each time a jump ("pulse") of the base pressure. The pressure in the reactor (base pressure) was set by a diaphragm pressure gauge (Baratron) and a PC-driven needle valve allowing the flow of O_2, N_2, forming gas (FG, a mixture 90% N_2−10% H_2), or of pure H_2 through the reactor and thus setting the base pressure at the desired value. For the deposition, after loading the substrate, the reactor was evacuated down to $10^{−2}$ Torr. Then, the base pressure was set to 0.1 Torr and the Mo wire was heated. Hot-wire Mo oxide films were deposited by heating the molybdenum filament at 560 °C and at base pressures of 5 mTorr. The deposition rates were measured at 0.5 nm/s for the stoichiometric, and 0.25 nm/s for the reduced and hydrogenated Mo oxides. During deposition, the substrates remained near room temperature, depending on the deposition time, but never exceeding approximately 50 °C.

Raman, X-ray, and Ultraviolet Photoelectron Spectroscopy. Micro-Raman spectra were obtained on a Renishaw inVia Reflex microscope using an Ar^+ ion laser ($\lambda = 514.5$ nm) as excitation source. The laser beam was focused onto the samples by means of a 50×

objective and the laser power density was 0.4 mW/μm^2. All the Raman spectra of the samples were obtained on silicon wafers. To remove background signal, the spectrum of a clean silicon wafer was subtracted from all Raman spectra of the films. Cosmic ray lines were also removed from the spectra. Overlapped bands in specific areas of the Raman spectra were resolved using Gaussian functions to fit the data.

The valence band spectra of Mo oxides were evaluated after recording the ultraviolet photoemission (UPS) spectra of 10 nm thick films deposited on ITO substrate, taken from the same batch used for OLEDs fabrication. For the UPS measurements, the HeI (21.22 eV) excitation line was used. A negative bias of 12.28 V was applied to the samples during UPS measurements in order to separate the sample, analyze high binding energy (BE) cutoffs, and estimate the absolute work function value from the high BE cutoff region of the UPS spectra. The analyzer resolution is determined from the width of the Au Fermi edge to be 0.16 eV. The unmonochromatized Mg Kα line at 1253.6 eV (15 keV with 20 mA anode current) and an analyzer (Leybold EA-11) pass energy of 100 eV, giving a full width at half-maximum (fwhm) of 1.3 eV for the Au 4f $_{7/2}$ peak, were used in all X-ray photoelectron spectroscopy (XPS) measurements. The oxide stoichiometry was estimated using the XPS-measured Mo 3d and O 1s core-level spectra. To this end, the areas under the photoemission peaks were integrated by fitting the O 1s and Mo 3d spectra with asymmetric Gaussian−Lorentzian curves. The error is estimated at ±10% in all the XPS-derived atomic percentages.

Film Optical and Electrical Characterization. Transmittance and absorption measurements were taken using a Perkin-Elmer Lampda 40 UV/vis spectrophotometer. The film resistance was measured using the four-point probe method with a dedicated Keithley meter.

Device Fabrication and Characterization. OLEDs and OPVs were fabricated on ITO-coated glass substrates (2 × 2 cm) with a sheet resistance 20 Ω/sq, which served as the anode electrode. Substrates were ultrasonically cleaned with a standard solvent regiment (15 min each in acetone and isopropyl alcohol). In OLEDs, the Mo oxide layer was then deposited followed by an approximately 70 nm thick emissive layer (EML) of the green-emitting copolymer poly[(9,9-dioctylfluorenyl-2,7-diyl)-*co*-(1,4-benzo-{2,1′,3}-thiadiazole)] (F8BT), spin-coated from a chloroform solution (at a concentration of 6 mg/mL). After deposition, the EML layer was annealed at 80 °C for 10 min in air. F8BT was purchased from American Dye Source and used as received. Then, in some devices, a thin polyoxometalate (POM) layer was deposited from a solution in methanol, on top of the EML to serve as an electron injection/transport layer. The devices were completed with a 150 nm thick aluminum cathode, deposited in a dedicated chamber. Film thickness was estimated with ellipsometry. The position of the F8BT HOMO level on different stoichiometry oxides was extracted from near-Fermi level UPS measurements of ultrathin F8BT films (less than 10 nm thickness), deposited from very dilute (<1 mg/mL) solutions on top of the oxide films. For OPVs, the active layer was a blend (1:0.8 wt %) of poly(3-hexylthiophene) (P3HT) and [6,6]-phenyl-C71-butyric acid methyl ester (PCBM-71), which was spin-coated from a 10 mg/mL chloroform solution to form a 100 nm thick film. After deposition the active layer was annealed at 125 °C for 10 min.

■ RESULTS AND DISCUSSION

Mo Oxides Preparation and Electronic Structure Evaluation Using Raman and Photoelectron Spectroscopy. The first major challenge of this study was the preparation and characterization of Mo oxide films of various stoichiometries and hydrogen contents. To identify Mo oxides' structure, Raman spectroscopy was performed on several films formulated in different environments. From Figure 1 it is deduced that deposition of Mo oxides in environment, with and without hydrogen, produces different reduced oxides. The Mo oxide film deposited in oxygen environment (curve a) shows three main characteristic bands (deconvoluted peaks): at 956
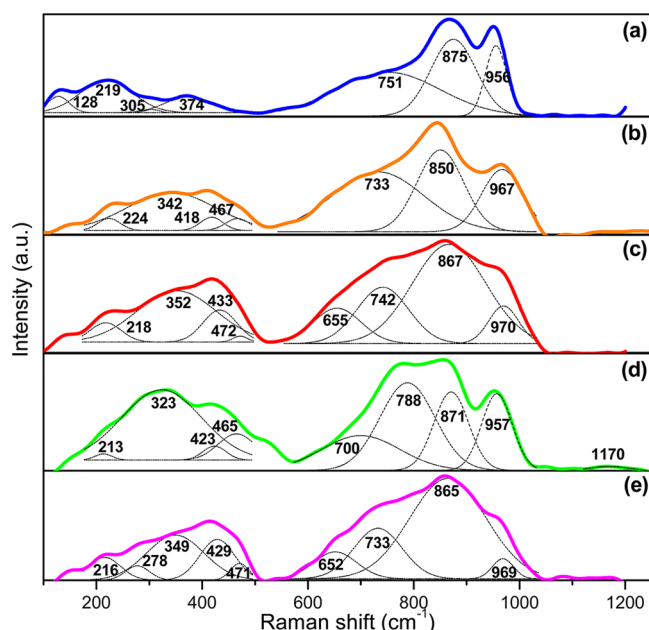
Figure 1. Raman spectra of the prepared molybdenum oxide films: (a) MoO_3, deposited in oxygen environment; (b) MoO_{3-x1}, deposited in nitrogen; (c) $H_{y1}MoO_{3-x2}$, deposited in forming gas (90% N_2 and 10% H_2, FG); (d) $H_{y2}MoO_{3-x3}$, deposited in pure hydrogen and (e) $H_{y3}MoO_{3-x4}$, deposited in FG while injecting H_2 pulses toward the filament. The deposition time was set in order for all Mo oxide films to have a thickness of 50 nm.

cm^{-1}, assigned to the stretching vibration of terminal oxygens ($\nu O{=}Mo$); at 875 cm^{-1}, assigned to the stretching mode of doubly coordinated oxygens ($\nu O{-}Mo_2$); and at 751 cm^{-1}, attributed to the stretching mode of triply coordinated oxygens ($\nu O{-}Mo_3$).[52−56] By applying mild reduction conditions (nitrogen environment, curve b), the band of the doubly coordinated oxygens considerably shifts to lower wavenumbers ($875{\rightarrow}850$ cm^{-1}; $\Delta\nu = -25$ cm^{-1}) in relation to the smaller shift observed for both terminal ($956{\rightarrow}967$ cm^{-1}; $\Delta\nu = 11$ cm^{-1}) and triply coordinated oxygens ($751{\rightarrow}733$ cm^{-1}; $\Delta\nu = -18$ cm^{-1}). Furthermore, a new band at 342 cm^{-1} appears. Raman spectra with similar but progressively larger band shifts were obtained for films deposited in a forming gas (FG)-containing environment (curve c) and especially when hydrogen pulses were injected toward the filament (curve, e), that is, the shift of the doubly coordinated oxygens band is $\Delta\nu = -125$ and -132 cm^{-1} and of the terminal oxygens $\Delta\nu = 14$ and 13 cm^{-1}, respectively. Also the new band at the region of 340−350 cm^{-1} appears stronger in intensity. On the other hand, the picture of the Raman spectrum is clearly different for a Mo oxide film deposited in pure hydrogen (curve d), showing similarities with the Raman spectrum of a hydrogenated film with the spillover technique (see Supporting Information, Figure S1). In particular, the band of the doubly coordinated oxygens shows a considerably smaller shift to lower wavenumbers ($871{\rightarrow}788$ cm^{-1}; $\Delta\nu = -83$ cm^{-1}), whereas the band of the terminal oxygens only decreases in intensity, without presenting a significant shift. In addition, the band at ca. 350 cm^{-1} does not appear in this case. Moreover, a new band at ca. 1170 cm^{-1} attributed possibly to the deformation mode of Mo−O−H bonds ($\delta Mo{-}O{-}H$) appears, a result confirmed also by FT-IR (Supporting Information, Figure S2) and in agreement with the literature.[69−74] The considerable shift of the

Mo−O−H band observed in this case is comparable to the band position reported in literature (1170 vs 1267 cm^{-1}, respectively) and could be attributed to the more amorphous structure of the molybdenum oxide films that are formed in the present work.[54]

According to the above Raman spectra, a similar reduction mechanism can be deduced for all films deposited in hydrogen-poor environment (N_2, FG) (curves b, c, and e). It is possible that the reduction in these films proceeds primarily through the formation of oxygen vacancies localized mainly in the doubly coordinated oxygens, a mechanism that is responsible for the increased substoichiometry of those films (vide infra). The creation of the new band at 340−350 cm^{-1} could be attributed to the stretching mode of Mo−Mo bonds, formed in the distorted lattice of the oxygen-deficient oxides, as reported previously.[57,58] However, in hydrogen-rich environment (curve d), the reduction mechanism proceeds probably, apart from the formation of vacancies upon removal of bridging oxygens, also through hydrogen incorporation in the terminal oxygens.[69,74,75] Note that the Mo oxide deposited in FG with the simultaneous injection of H_2 pulses (curve e) was highly reduced, probably through a two-step mechanism: First, hydrogenation and sequential removal of neighbor hydroxyl groups in the form of water, followed by the formation of highly reduced species (e.g., MoO_2), as reported previously in the literature.[69,70]

To further shed light on the reduction mechanism and correlate their stoichiometry with their electronic properties (such as work function and gap states), photoemission measurements were performed. The percentage of the various Mo oxidation states (Mo^{6+}, Mo^{5+}, Mo^{4+}) in these films was evaluated by XPS. The chemical composition of each film was determined by analyzing the XPS spectra of the Mo 3d core level peaks shown in Figure 2. Oxide identification is accomplished from the shift of the Mo 3d core levels with regard to its stoichiometric form and by calculating the ratio between the Mo^{6+} component versus the Mo components with lower oxidation states (5+ and 4+). A summary of the different Mo oxides formulated in this study is shown in Table 1, along with the percentage of various oxidation states of the Mo cation. From these data, it can be deduced that the degree of oxide reduction increases in the sequence $MoO_3 < MoO_{3-x1} < H_{y1}MoO_{3-x2} < H_{y2}MoO_{3-x3} < H_{y3}MoO_{3-x4}$. Indeed, the Mo 3d core level spectrum of the MoO_3 (curve a) consists of a spin−orbit doublet with peaks at 232.4 and 235.7 eV BE, associated with Mo cations in the higher oxidation state (Mo^{6+});[38,39,59] thus, the formulated oxide indeed corresponds to the fully stoichiometric compound. The Mo 3d core level spectrum of the substoichiometric oxide MoO_{3-x1} (curve b) is considerably broader and the initially, well-defined, doublet evolves to a less-structured shape, whereas the presence of the Mo^{5+} lower oxidation state (Mo $3d_{5/2}$ at 231.6 eV and Mo $3d_{3/2}$ at 234.9 eV BE), accounting for 15% of the total Mo states, is evident. The Mo 3d core level spectrum of the hydrogenated oxide $H_{y1}MoO_{3-x2}$ (curve c) is similar to that of MoO_{3-x1} but it exhibits an increased ratio of Mo^{5+} oxidation states, now accounting for 25% of the total Mo states, whereas for $H_{y2}MoO_{3-x3}$ an even higher portion of 35% of the Mo cations are in the Mo^{5+} state (curve d). Further reduction led to a spectrum dominated by three overlapping spin−orbit doublets (curve e). Apart from the initial Mo^{6+} (50% of the total Mo cations) and the Mo^{5+} (accounting for the 30% of the total), the appearance of the lowest oxidation Mo^{4+} state (peaks at
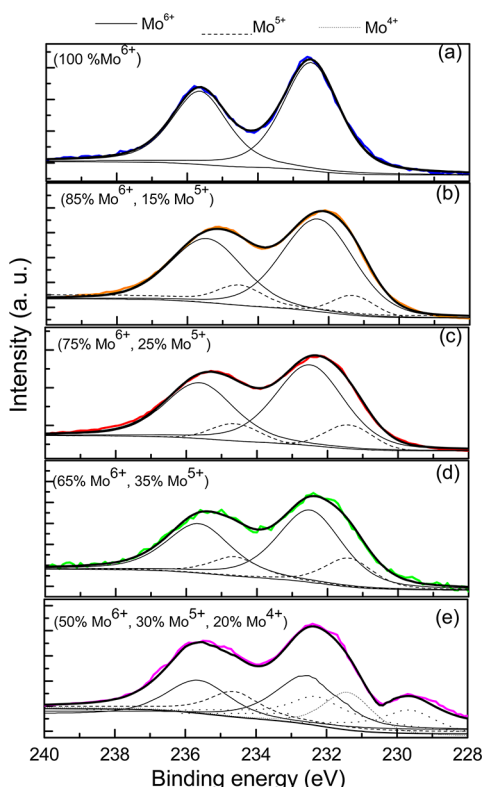
Figure 2. XPS Mo 3d core level spectra of (a) MoO_3, (b) MoO_{3-x1}, (c) $H_{y1}MoO_{3-x2}$, (d) $H_{y2}MoO_{3-x3}$, and (e) $H_{y3}MoO_{3-x4}$. The oxides were prepared under the same conditions (i.e., having the same thickness) as in the Raman measurements.

229.1 and 232.3 eV BE),[60,61] in a portion of 20% of the Mo cations, can be observed.

The O 1s photoemission peaks (Figure 3) are not nearly as useful in identifying oxides as are the Mo peaks. The O 1s BE for all TMOs are generally between 529.5 and 530.5 eV. The XPS O 1s spectra of MoO_3 and MoO_{3-x1} (curves a and b) are found to peak at 530.4 eV BE and are assigned to the typical Mo−O bond.[60] However, the deconvolution process in the O 1s region of the hydrogenated Mo oxides reveal an extra peak (beyond the typical oxide region) at 531.5 eV BE, which could be assigned to hydroxyl groups (−OH) incorporated within the lattice.[60,74] Furthermore, the O 1s XPS spectrum broadens (increasing fwhm) as the hydrogen content in the deposition environment increases (i.e., the largest, by far, hydroxyl group formation is observed for $H_{y2}MoO_{3-x3}$, which was deposited in pure hydrogen). Moreover, a slight overall shift toward higher BEs can be detected which may be indicative of oxygen removal from the oxide lattice.

Further studies on the electronic structure of Mo oxides prepared at different deposition environments were performed
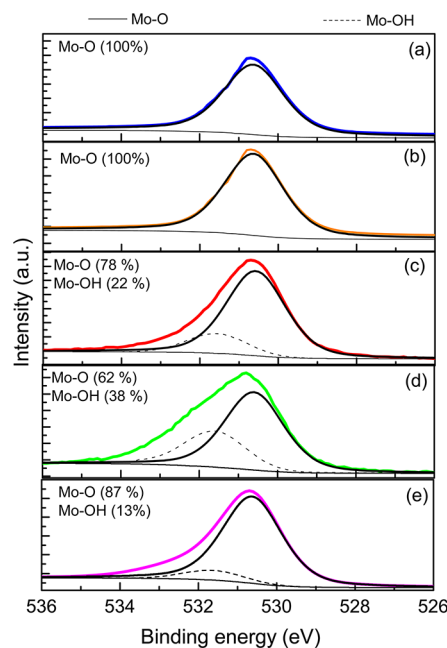

Figure 3. O 1s XPS spectra of (a) MoO_3, (b) MoO_{3-x1}, (c) $H_{y1}MoO_{3-x2}$, (d) $H_{y2}MoO_{3-x3}$, and (e) $H_{y3}MoO_{3-x4}$.

by UPS. The valence band spectra are shown in Figure 4a, whereas the expanded view of the valence band and the high BE cutoff region are shown separately in Figures 4b and c, respectively. The UPS spectrum of MoO_3 is structureless and exhibits only a single peak, as expected for amorphous molybdenum trioxide.[62] Its valence band consists mainly of O 2p orbitals with its edge located at about 3 eV below the Fermi level. On the other hand, Mo oxide films prepared in reducing environments exhibit very similar UPS spectra with an increased fwhm compared to that of the stoichiometric film.[60] The most striking difference between the UPS line shape in the reduced Mo oxides versus the stoichiometric one is the appearance of new broad features near the E_F,[63] which are not observed in the case of MoO_3. A single new peak appears in the case of oxygen-deficient MoO_{3-x1} centered at 2.2 eV. However, in the case of hydrogenated Mo oxides and especially in those with the highest hydrogen content (namely the $H_{y1}MoO_{3-x2}$ and $H_{y2}MoO_{3-x3}$), apart from the peak at 2.2 eV, a second one, closer to the Fermi level (centered at 1.1 eV) grows, approaching in intensity/width the one at 2.2 eV. These bands are indicative of new occupied states forming inside the band gap with a relatively large density (the origin of which is discussed below).

Figure 4c shows the evolution of the high BE cutoff region of the UPS spectra for the above Mo oxides. The MoO_3 work function (W_F) is about 6.2 eV, which is lower than that of vacuum-deposited stoichiometric Mo oxide film,[23] but in

Table 1. Synopsis of Electronic Properties of the Mo Oxides Deposited at Different Conditions

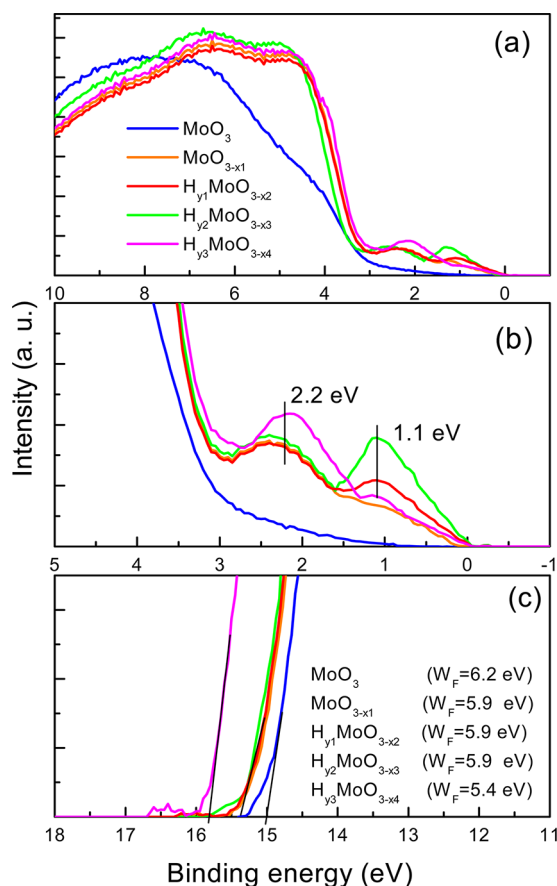|	deposition environment (%)			XPS Mo 3d core levels (%)			XPS O 1s peak	
	O_2	N_2	H_2	Mo^{6+}	Mo^{5+}	Mo^{4+}	OH^-/O_2^-	oxide work function (eV)
MoO_3	100	−	−	100	0	0	0	6.2
MoO_{3-x1}	−	100 (1O₂ pulse)	−	85	15	0	0	5.9
$H_{y1}MoO_{3-x2}$	−	90	10	75	25	0	0.22	5.9
$H_{y2}MoO_{3-x3}$	−	−	100	65	35	0	0.38	5.9
$H_{y3}MoO_{3-x4}$	−	90 (+2H₂ pulses)	10	50	30	20	0.13	5.4

Figure 4. UPS photoemission spectra of the Mo oxides prepared in this study: (a) valence band spectra, (b) near E_F region valence band and (c) secondary-electron cutoff region.

accordance with values reported in the literature for samples that have been exposed to ambient.[25] For the Mo oxides prepared in reducing environment, lower W_F values were measured (results shown in Table 1), depending on both the degree of reduction (the highly reduced $H_{y3}MoO_{3-x4}$ film exhibits the lowest W_F equal to 5.4 eV) and the hydrogen content (the highly hydrogenated $H_{y2}MoO_{3-x3}$ exhibits W_F equal to the substoichiometric, MoO_{3-x1}, despite the fact that its degree of reduction is higher).

To correlate the main differences observed in Raman, XPS and UPS spectra of the different Mo oxides with their preparation conditions, a short discussion regarding the oxides band structure is necessary. According to the band structure based on the one developed by Goodenough for ReO_3[64−67] and adapted to MoO_3, in a discrete MoO_6 unit the Mo 4d orbitals with e_g symmetry overlap with six sp hybrid orbitals of the oxygen atom to give a set of six bonding σ and six antibonding σ^* molecular orbitals. In the extended lattice, the discrete energy levels arising from this unit structure will broaden into bands (see Supporting Information, Figure S3 for the detailed schematic representation of the MoO_3 band structure). The Mo 4d orbitals with the lower t_{2g} symmetry can overlap with three of the surrounding oxygen p_π orbitals per octahedron to form bonding π and antibonding π^* bands. The π and σ bands are filled and constitute the valence band separated by a large gap (3.2 eV in our case, see also Supporting Information, Figure S4) from the conduction band constituted of π^* and σ^* bands. The conduction band is empty in MoO_3, so this material is a wide bandgap semiconductor, practically an insulator (Figure 5a, left). In the case of oxygen-deficient (MoO_{3-x}) Mo oxides, a portion of the electrons coming from the oxygen vacancies (two electrons per oxygen vacancy) are transferred to the initially empty π^* band, located partially at the edge of the conduction band and partially within the band
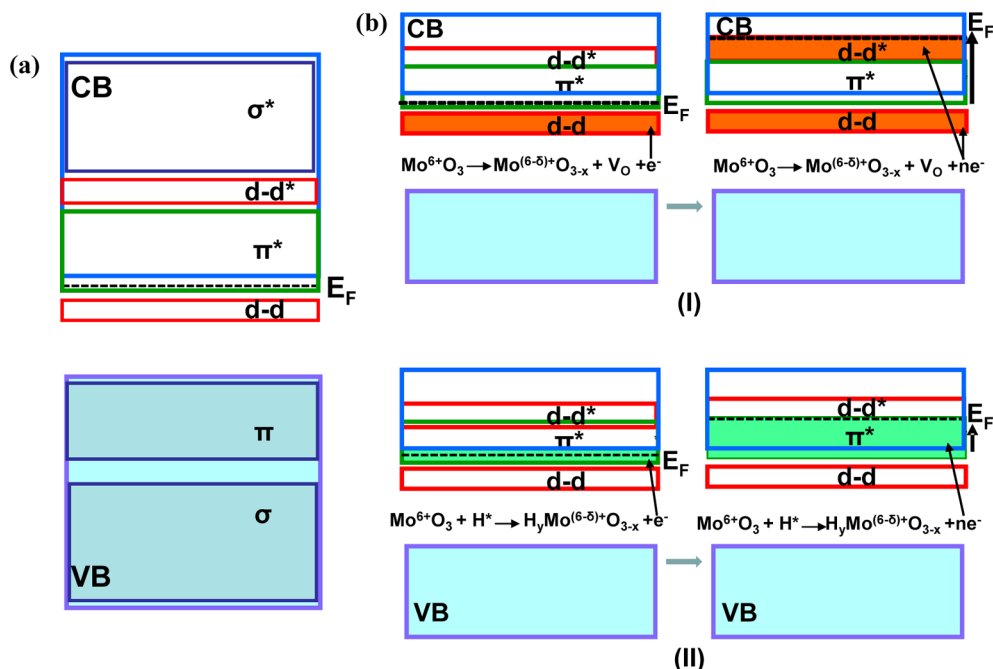

Figure 5. (a) Band structure of MoO_3 where occupied orbitals with dominant O 2p character comprise the VB, while empty orbitals with mainly Mo 4d character comprise the CB. The d−d bands attributed to Mo−Mo bonds formed in the distorted lattice of the oxygen-deficient Mo oxides are also shown. (b) Schematic illustration of the evolution of gap states occupation and Fermi level movement toward higher binding energy in Mo oxide (I) with the progress of oxygen vacancy formation in hydrogen-poor reducing environments and (II) with the evolution of hydrogenation.

gap, near the Fermi level.[65] However, for a portion of the freely vibrating electrons, an increased probability exists to be found near the neighboring Mo atoms and, thus, to be transferred to the Mo−Mo (with d−d character) bands.[65,67,68] These bands are formed upon oxygen removal from the lattice, which permits the direct overlapping of the Mo 4d orbitals, and they are lying within the bandgap, the bonding one, and near the edge and within the conduction band, the antibonding one.

For low degrees of reduction, the bonding d−d band is partially occupied by electrons (this effect results in the appearance of gap states at 2.2 eV BE), so the Fermi level is positioned within the band gap (Figure 5a, middle). At higher degrees of reduction, electrons start to occupy the antibonding d−d band and the Fermi level is shifted within the conduction band, resulting in a considerable decrease of the oxide work function (Figure 5a, right). In the case of oxide reduction using atomic hydrogen, except for oxygen vacancies, the formation of hydroxyl groups has also been reported.[69−74] Hydrogen atoms can form strong covalent bonds with bridging[72] and mainly with terminal oxygen atoms.[73−75] As a result, intervalence electron transfer in the previously empty π^* band, located near the CB edge (depicted as gap states appearing at 1.1 eV BE), occurs. Upon increasing the degree of hydrogenation, which results in progressive occupation of the π^* band, no significant shift of the Fermi level is expected and the oxides work function remains nearly identical to that of MoO_3 (Figure 5 b). Indeed, this is the case for the highly hydrogen doped $H_{y2}MoO_{3-x3}$, which maintains a high W_F of 5.9 eV (only 0.3 eV lower than that of MoO_3), despite the fact that its degree of reduction is much larger than that of the oxygen-deficient MoO_{3-x1} film with the same W_F value. However, it should be mentioned that since all Mo oxide films are exposed to air before having their work functions measured, alterations in the measured W_F should be expected (e.g., an error of no better than ±0.2 eV is possible).

Conductivity and Transmission Measurements in Mo Oxide Films. To examine electron transport in oxygen-deficient and hydrogenated Mo oxide films, we investigated the temperature dependence of their electrical resistivity in 10 nm thick films, and the results are shown in Figure 6a. A gradual decrease of the resistivity with the degree of reduction can be clearly seen. At room temperature, the resistivity drops nearly 3 orders of magnitude for the hydrogenated Mo oxides with the highest hydrogen content (namely, $H_{y1}MoO_{3-x2}$ and $H_{y2}MoO_{3-x3}$), resulting in enhanced conductivity and improved charge transport properties. Moreover, the highly reduced $H_{y3}MoO_{3-x4}$ oxide film seems to be nearly metallic, with its resistivity at room temperature almost 4 orders of magnitude lower than the corresponding value of the stoichiometric one (6×10^{-2} vs 5×10^2 Ω·cm). The progressive transition from semiconducting to metallic behavior is evidenced by the dependence of the oxide resistivity on temperature. The resistivity of the highly reduced Mo oxide increases with temperature, which is evidence for metallic-like behavior, while for MoO_3 and MoO_{3-x1}, semiconducting dependence was observed (i.e., decrease with temperature).

Despite the creation of bandgap states, all Mo oxide films were found to be highly transparent in thicknesses less than 10 nm, as one can see in Figure 6b, and, thus, appropriate for use as interfacial layers at the anode side of optoelectronic devices, where the light extraction/insertion occurs. We chose though to keep the thickness of all Mo oxide films fixed at 5 nm in order to achieve an optical transparency of more than 90% in the visible spectrum region. (More characterization results
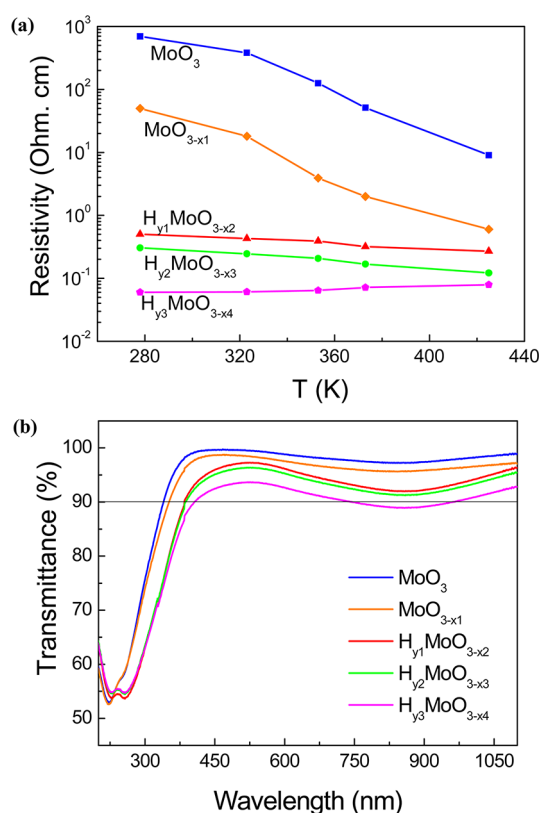

Figure 6. (a) Resistivity measurements vs temperature and (b) transmission spectra of 10 nm thin Mo oxide films.

regarding other optical parameters such as the dispersion of their refractive indices and extinction coefficients are given in Supporting Information, Figures S5 and S6.) It should also be mentioned that hydrogenated films exhibited smoother morphologies than the stoichiometric and the oxygen-deficient ones (see Supporting Information, Figures S7 and S8). Since the surface morphology of films used at the interface with an electrode and organic material may affect the charge injection/transport process, smooth surface can be beneficial for the performance of optoelectronic devices. Furthermore, the environmental stability of the oxygen-deficient and hydrogenated films was also tested in a period of 900 h. It was found that the incorporation of hydrogen within the lattice may play a stabilizing role in oxide stoichiometry and structural integrity, since the reduction in the absorbance of $H_{y2}MoO_{3-x3}$ was less than 20% within this period of time, whereas for the MoO_{3-x1} film, the corresponding changes reached 50% (see Supporting Information, Figure S9). Nevertheless, further investigation is needed to evaluate this behavior.

Performance of Organic Optoelectronic Devices with Different Mo Oxides as Anode Interfacial Layers. *a. OLEDs.* Having now a direct correlation of the Mo oxide films preparation conditions with their electronic structure and physical properties, we employed these oxides as anode interfacial layers in OLEDs. The fabricated device structure was ITO/Mo oxide/F8BT (as the emissive layer)/POM/Al, where POM is the 12-phosphotungstic acid ($H_3PW_{12}O_{40}$),[76] a polyoxometalate previously reported from our group as a highly efficient electron injection layer (EIL), which can be cast from alcohol-based orthogonal solvents with regard to the polymeric layer underneath. In Figure 7a, the current density−voltage−luminance (J−V−L) characteristics for devices with a 5 nm thin
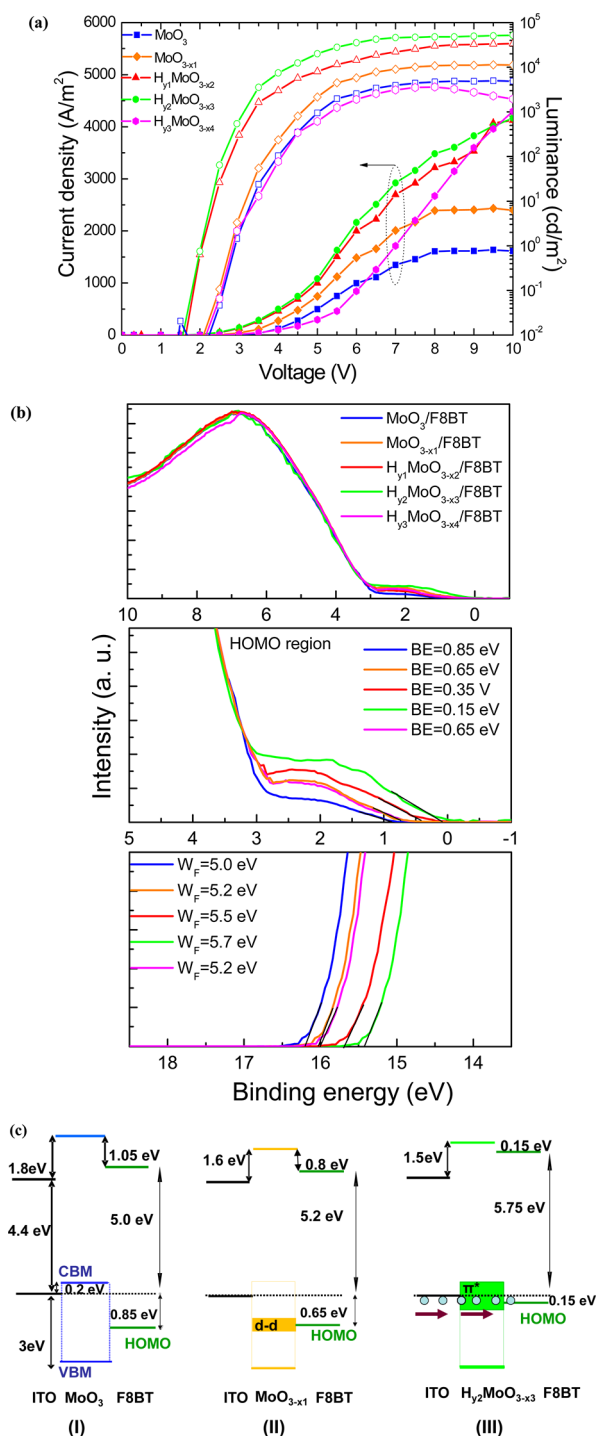
Figure 7. (a) Current density−voltage (solid symbols) and luminance−voltage (open symbols) characteristic curves of OLEDs with the structure ITO/Mo oxides (5 nm)/F8BT/POM (2 nm)/Al devices. (b) UPS spectra of thin (~5 nm) F8BT layers deposited on top of the different Mo oxides (upper), near the E_F valence band region (middle), and at the high BE cutoff region (lower). (c) Energy level alignment at the ITO/Mo oxide/F8BT interface in the case of the stoichiometric (left), oxygen-deficient (middle), and hydrogenated (right) Mo oxides. Hole injection barriers and interfacial dipoles are also shown; the hole injection mechanism is also illustrated in the latter case. Blue cycles are symbols for holes.

Mo oxide film as HIL and a ~2 nm thin polyoxometalate (POM) EIL are shown. Results are summarized in Table 2 and

detailed efficiencies are depicted in Figure S10 in Supporting Information. In the MoO_3-based device, a rather large turn-on voltage (voltage where light emission is equal to 10 cd/m^2) of about 3.5 V and overall low light emission (with a peak luminance of 5000 cd/m^2) is observed. On the contrary, in the oxygen-deficient and especially in the hydrogenated Mo oxide-based devices, almost 1 order of magnitude higher peak luminances are obtained, accompanied by a large decrease in the device turn-on and operating voltage. In particular, the device with the $H_{y2}MoO_{3-x3}$ reaches luminance up to 45 000 cd/m^2 and current densities of 4300 A/m^2, while it also exhibits a low turn-on voltage of 2.5 V. The peak current efficiency of 10.5 cd/A represents one of the best values reported for thin (<100 nm) F8BT-based OLEDs.[77,78] However, the device with the Hy_3MoO_{3-x4} (with the largest degree of reduction and the lowest work function) exhibited rather poor performance, as expected, since the oxide work function has become ~0.45 eV lower than the F8BT's ionization energy (~5.85 eV, see next paragraph), and thus, the previously favorable interfacial energy alignment, originated from the high W_F of the other Mo oxides, is disrupted.[37,38] It should be mentioned that the stability of the devices operating in air was tested in a period of 700 h and was excellent for all the Mo oxide-based devices (see Supporting Information, Figure S11).

To clarify the origin of high efficiencies and low voltages obtained in OLEDs with the hydrogenated $H_{y1}MoO_{3-x2}$ and, especially, $H_{y2}MoO_{3-x3}$ films as anode interfacial layers and unravel the hole injection mechanism, we conducted UPS measurements for the determination of the HOMO position of a thin F8BT layer (less than 10 nm) on each one of the Mo oxides. The energy difference between the E_F and the HOMO edge of F8BT on each oxide corresponds to the hole injection barrier at the HIL/F8BT interface.[38] These UPS results are shown in Figure 7b (upper), where the expanded valence band region (middle) and the high BE cutoff region (lower) are also shown. As it can be seen, the position of the F8BT HOMO edge with regard to the E_F depends on the composition of the oxide underlayer. The F8BT HOMO on MoO_3 is located about 0.85 eV below the E_F, resulting in a very large hole injection barrier. The HOMO of F8BT on the oxygen-deficient MoO_{3-x1} shifts about 0.2 eV closer to the E_F (BE ~0.65 eV), and on the $H_{y1}MoO_{3-x2}$ shifts 0.3 eV further (BE ~0.35 eV), whereas that on the $H_{y2}MoO_{3-x3}$ is only 0.15 eV below the E_F, leading essentially to a close to zero barrier for hole injection (i.e., ohmic contact).[30] However, on $H_{y3}MoO_{3-x4}$ (the Mo oxide with the highest degree of reduction and the lowest work function), the HOMO of F8BT is shifted away from the E_F again, ~0.65 eV below it, thus resulting in a significant energy level offset and a large hole injection barrier. Note that a large interfacial dipole (~1.2 eV) is initially formed in the MoO_3/F8BT interface which generally decreases with the evolution of reduction. From the work function and the HOMO position, the ionization energy of F8BT was calculated to be 5.85 eV, in accordance with literature values.[78]

The above results provide comprehensive evidence for the decrease of the hole injection barrier in the hydrogenated, moderately reduced, Mo oxide/F8BT interfaces which results in a highly favorable interfacial energy alignment. In addition, the creation of the gap states near the Fermi level is expected to be beneficial for charge transport. Thus, the $H_{y2}MoO_{3-x3}$ oxide (deposited in pure hydrogen) exhibiting both the highest work function and the largest density of occupied gap states near the Fermi level is proposed to result to near barrierless hole

Table 2. Device Characteristics of OLEDs Having the Structure ITO/Mo Oxide (HIL)/F8BT/POM (EIL)/Al

HIL	$V_{turn-on}$ (V) (at 10 cd/m^2)	J (A m^{-2})	L_{max} (cd m^{-2})	max current efficiency (cd A^{-1}) [at voltage]	max power efficiency (lm W^{-1}) [at EQE]
MoO$_3$	3.5	1500	5000	3.0 (5.0 V)	1.9 (1.0%)
MoO$_{3-x1}$	3.0	2500	11500	4.6 (5.0 V)	2.9 (1.5%)
H$_{y1}$MoO$_{3-x2}$	2.5	4000	35000	8.5 (4.5 V)	6.5 (3.0%)
H$_{y2}$MoO$_{3-x3}$	2.5	4300	45000	10.5 (4.5 V)	7.3 (3.5%)
H$_{y3}$MoO$_{3-x4}$	3.0	4400	3500	3.2 (5.0 V)	2.0 (1.1%)

injection and largely enhanced charge transport at the Mo oxide/F8BT interface. In Figure 7c, the energy level alignment at the Mo oxide/F8BT interface in the case of stoichiometric, oxygen-deficient (MoO$_{3-x1}$), and hydrogenated (H$_{y2}$MoO$_{3-x3}$) Mo oxide films is shown. Moreover, the nearly zero barrier for hole injection in the case of the H$_{y2}$MoO$_{3-x3}$/F8BT interface through favorable energy alignment and the enhanced hole transport via the gap states near the E_F are also illustrated.

b. OPVs. Finally, we investigated the effect of incorporating the Mo oxide-based formulations described previously as hole extraction/transport (HEL/HTL) layers in P3HT:PCBM[71] (1:0.8 wt/%) bulk heterojunction solar cells. Current-density−voltage (J−V) characteristics under simulated 1.5G solar irradiation are shown in Figure 8a, while Table 3 summarizes the device operational characteristics. A significant improvement in the short circuit current (J_{sc}), the open circuit voltage (V_{oc}), the fill factor (FF), and the cell power conversion efficiency (PCE) was achieved for substoichiometric Mo oxides, compared to the stoichiometric MoO$_3$ HEL. In particular, V_{oc} increases from 0.53 V for MoO$_3$ to 0.69 V when the hydrogenated H$_{y2}$MoO$_{3-x3}$ oxide is used as the HEL. This represents a 30% improvement for the device incorporating the substoichiometric Mo oxide with the highest amount of hydrogen approaching the theoretical limit of ∼0.7 V for a P3HT:PCBM solar cell with ohmic contacts.[79,80] This large increase in V_{oc} is attributed to a more favorable energy alignment obtained at the ITO/Mo oxide/polymer blend interface via the formation of an ohmic contact, as a result of the higher work function of this oxide compared to the ionization energy of P3HT, that enhances the cell built-in potential and facilitates barrier-free hole extraction. Similarly, the J_{sc} increases by a factor of 2 (from 5.68 to 11.64 mA/cm^2) and the FF increases from 0.32 to 0.54 (almost a 70% improvement). The large enhancement of both the J_{sc} and the FF is reflected in the considerable reduction of the series resistance (R_s from 50 to 7.5 Ω·cm^2) and the moderate increase of the shunt resistance (R_{sh} from 202 to 300 Ω·cm^2) of the substoichiometric Mo oxide modified cell, clearly suggesting a reduced contact resistance, improved hole transport through gap states, and reduced leakage currents, respectively. The significant improvement of all the solar cell parameters results in a dramatic increase of the PCE to 4.34%, compared to only 0.96% for the MoO$_3$-based cell (a more than a factor of 4 enhancement). However, device efficiency is reduced significantly to 1.19% when the highly reduced, lower work function, H$_{y3}$MoO$_{3-x4}$ oxide is used. This is primarily reflected as a significant reduction of the FF of the solar cell to 0.24 (a ∼55% decrease) whereas a smaller decrease of the J_{sc} (8.43 mA/cm^2) and V_{oc} (0.59 V) also occurs. The large decrease of the FF is attributed to the huge increase of the cell series resistance and the significant decrease of its shunt resistance, whereas the appearance of a slight kink in the J−V curve in the fourth quadrant becomes evident. The reduction of J_{sc} and V_{oc} is
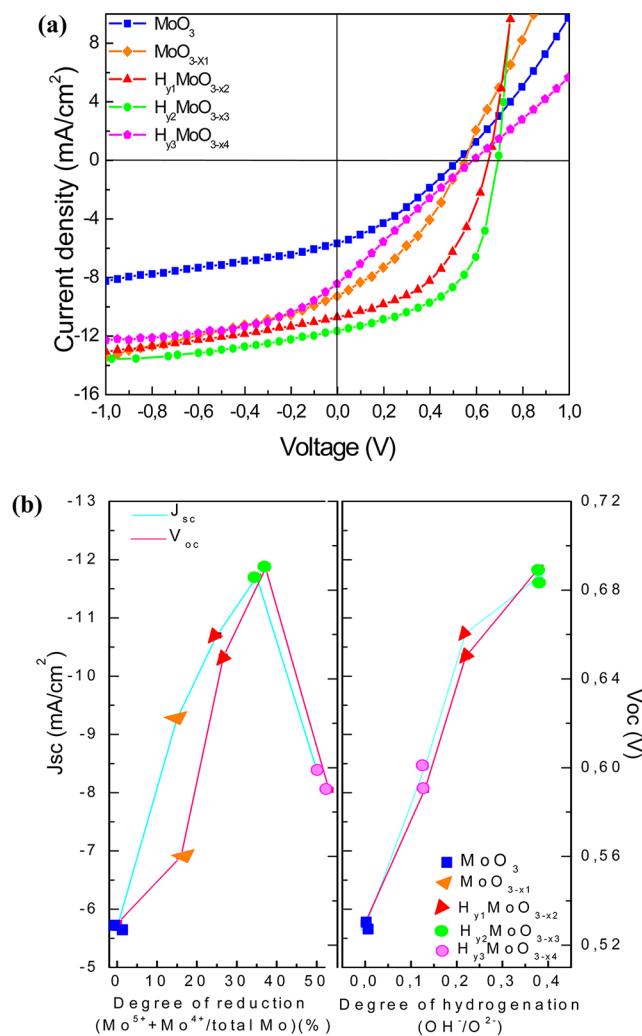

Figure 8. (a) Current density versus voltage characteristics for P3HT:PCBM[71] BHJ devices embedding 5 nm Mo oxide hole extracting layers. (b) Variation of J_{sc} and V_{oc} with the degree of reduction (the portion of Mo atoms with oxidation states 5+ and 4+ relative to the total Mo cations, as derived from 3d Mo XPS measurements) and the hydrogen content (the amount of Mo−OH relative to Mo−O bonds, as derived from O 1s XPS results), respectively.

primarily attributed to the disruption of the favorable energetic alignment at the oxide/P3HT blend interface, as a result of the significantly lower work function of this Mo oxide that is pinned close to the P3HT HOMO.

Therefore, the degree of oxide reduction (expressed by the ratio of lower Mo oxidation states Mo^{5+} and Mo^{4+} in the film) and the amount of hydrogen doping are highly critical for optimal solar cell performance as shown in Figure 8b, where the J_{sc} and V_{oc} values are plotted versus the degree of reduction of

Table 3. Device Characteristics of BHJ Organic Solar Cells with the Structure ITO/Mo Oxide (HEL)/P3HT:PC71BM/Al

HEL	J_{sc} (mA/cm^2)	V_{oc} (V)	FF	PCE (%)	R_s ($\Omega \cdot$cm^2)	R_{sh} ($\Omega \cdot$cm^2)
MoO$_3$	5.68	0.53	0.32	0.96	50	202
MoO$_{3-x1}$	9.28	0.56	0.35	1.82	28	123
H$_{y1}$MoO$_{3-x2}$	10.71	0.65	0.48	3.34	10	264
H$_{y2}$MoO$_{3-x3}$	11.64	0.69	0.54	4.34	7.5	300
H$_{y3}$MoO$_{3-x4}$	8.43	0.59	0.24	1.19	73	79

Mo atoms and the hydrogen content, respectively. Both J_{sc} and V_{oc} show a monotonic increase with regard to the hydrogen doping content in the hydrogenated film. On the other hand, a significant progressive enhancement of both J_{sc} and V_{oc} as the degree of reduction of Mo atoms increases is followed, after both reaching maxima values for ∼30% ratio of (Mo$^{\delta+,\delta<6}$)/Mo^{6+} atoms, by a large decrease when this ratio increases further. These results provide unambiguous evidence for the significant role of oxide work function, hydrogen incorporation in the metal oxides' lattice and degree of oxide reduction and their critical influence in solar cell performance.

CONCLUSIONS

In summary, we have shown that hydrogenated Mo oxides exhibit desirable electronic properties. The tuning of their electronic structure was achieved as a result of hydrogen incorporation within their lattice, evidenced through the hydroxyl group formation. Electrons from hydrogen dopant atoms are transferred to the π^* band located near the Fermi level in the energy gap, resulting in a small decrease of the oxides' work function. In the case of oxygen-deficient Mo oxides, electrons coming from oxygen vacancies occupy partly the bonding d−d band located deep in the forbidden gap, while in highly reduced oxides, the antibonding d−d* band occupation results in a large upward shift of the Fermi level and, thus, in a substantial decrease of the oxides' work function. As a consequence, the favorable energy alignment at the metal oxide/organic interface may be disrupted. The beneficial role of hydrogenation versus oxygen vacancy formation in Mo oxides for application in efficient organic electronic devices was demonstrated and attributed to (1) maintaining a large enough oxide work function, after its hydrogenation and (2) the occupation of gap states near the Fermi level, for highly efficient charge transfer to/from organic molecules. These findings demonstrate the tremendous potential of hydrogen incorporation in transition metal oxides and pave the way for new oxide formulations that can be used not only in organic optoelectronics, but also in additional diverse applications such as in photocatalysis and fuel cells.

ASSOCIATED CONTENT

Ⓢ Supporting Information

Additional figures and relevant discussion as noted in text. This material is available free of charge via the Internet at http://pubs.acs.org.

AUTHOR INFORMATION

Corresponding Author
mariva@imel.demokritos.gr

Notes
The authors declare no competing financial interest.

REFERENCES

(1) Forrest, S. R. *Nature* **2004**, *428*, 911.
(2) Tang, C. W.; Van Slyke, S. A. *Appl. Phys. Lett.* **1987**, *51*, 913.
(3) Burroughes, J. H.; Bradley, D. D. C.; Brown, A. R.; Marks, R. N.; Mackay, K.; Friend, R. H.; Burns, P. L.; Holmes, A. B. *Nature* **1990**, *347*, 539.
(4) Friend, R. H.; Gymer, R. W.; Holmes, A. B.; Burroughes, J. H.; Marks, R. N.; Taliani, C.; Bradley, D. D. C.; Dos Santos, D. A.; Brédas, J. L.; Lögdlund, M.; Salaneck, W. R. *Nature* **1999**, *397*, 121.
(5) Yu, G.; Gao, J.; Hummelen, J. C.; Wudl, F.; Heeger, A. J. *Science* **1995**, *270*, 1789.
(6) Blom, P. W. M.; Mihailetchi, V. D.; Koster, L. J. A.; Markov, D. E. *Adv. Mater.* **2007**, *19*, 1551.
(7) Dennler, G.; Scharber, M. C.; Brabec, C. J. *Adv. Mater.* **2009**, *21*, 1323.
(8) Ma, H.; Yip, H.-L.; Huang, F.; Jen, A. K.-Y. *Adv. Funct. Mater.* **2010**, *20*, 1371.
(9) Sessolo, M.; Bolink, H. J. *Adv. Mater.* **2011**, *23*, 1829.
(10) Nomura, K.; Ohta, H.; Takagi, A.; Kamiya, T.; Hirano, M.; Hosono, H. *Nature* **2004**, *432*, 488.
(11) Banger, K. K.; Yamashita, Y. Y.; Mori, K.; Peterson, R. L.; Leedham, T.; Rickard, J.; Sirringhaus, H. *Nat. Mater.* **2011**, *10*, 45.
(12) Matsushima, T.; Kinoshita, Y.; Murata, H. *Appl. Phys. Lett.* **2007**, *91*, 253504.
(13) You, H.; Dai, Y.; Zhang, Z.; Ma, D. *J. Appl. Phys.* **2007**, *101*, 026105.
(14) Bolink, H. J.; Coronado, E.; Orozco, J.; Sessolo, M. *Adv. Mater.* **2009**, *21*, 79.
(15) Haque, S. A.; Koops, S.; Tokmoldin, N.; Durrant, J. R.; Huang, J. S.; Brandley, D. D. C.; Palomares, E. *Adv. Mater.* **2007**, *19*, 683.
(16) Tokmoldin, N.; Griffiths, N.; Bradley, D. D. C.; Haque, S. A. *Adv. Mater.* **2009**, *21*, 3475.
(17) Bolink, H. J.; Coronado, E.; Repetto, D.; Sessolo, M.; Barea, E. M.; Bisquert, J.; Garcia-Belmonte, G.; Prochazka, J.; Kavan, L. *Adv. Funct. Mater.* **2008**, *18*, 145.
(18) Kabra, D.; Lu, L. P.; Song, M. H.; Snaith, H. J.; Friend, R. H. *Adv. Mater.* **2010**, *22*, 3194.
(19) Gwinner, M. C.; Di Pietro, R.; Vaynzof, Y.; Greenberg, K. J.; Ho, P. K. H.; Friend, R. H.; Sirringhaus, H. *Adv. Funct. Mater.* **2011**, *21*, 1432.
(20) Morii, K.; Ishida, M.; Takashima, T.; Shimoda, T.; Wang, Q.; Nazeeruddin, K.; Grätzel, M. *Appl. Phys. Lett.* **2006**, *89*, 183510.
(21) Wang, F.; Qiao, X; Xiong, T.; Ma, D. *Org. Electron.* **2008**, *9*, 985.
(22) Meyer, J.; Hamwi, S.; Schmale, S.; Winkler, T.; Johannes, H.-H.; Riedl, T.; Kowalsky, W. *J. Mater. Chem.* **2009**, *19*, 702.
(23) Kröger, M.; Hamwi, S.; Meyer, J.; Riedl, T.; Kowalsky, W.; Kahn, A. *Org. Electron.* **2009**, *10*, 932.
(24) Hamwi, S.; Meyer, J.; Kröger, M.; Winkler, T.; Witte, M.; Riedl, T.; Kahn, A.; Kowalsky, W. *Adv. Funct. Mater.* **2010**, *20*, 1762.
(25) Irfan; Ding, H.; Gao, Y.; Kim, D. Y.; Subbiah, J.; So, F. *Appl. Phys. Lett.* **2010**, *96*, 073304.
(26) Ma, H.; Yip, H.-L.; Huang, F.; Jen, A. K.-Y. *Adv. Funct. Mater.* **2010**, *20*, 1371.
(27) Matsushima, T.; Kinoshita, Y.; Murata, H. *Appl. Phys. Lett.* **2007**, *91*, 253504.
(28) Nicolai, H. T.; Wetzelaer, G. A. H.; Kuik, M.; Kronemeijer, A. J.; de Boer, B. P.; Blom, W. M. *Appl. Phys. Lett.* **2010**, *96*, 172107.
(29) Nakayama, Y.; Morii, K.; Suzuki, Y.; Machida, H.; Kera, S.; Ueno, N.; Kitagawa, H.; Noguchi, Y.; Ishii, H. *Adv. Funct. Mater.* **2009**, *19*, 3746.
(30) Wang, Z. B.; Helander, M. G.; Greiner, M. T.; Qiu, J.; Lu, Z. H. *Phys. Rev. B* **2009**, *80*, 235325.

(31) Greiner, M. T.; Helander, M. G.; Wang, Z. B.; Tang, W. M.; Qiu, J.; Lu, Z. H. *Appl. Phys. Lett.* **2010**, *96*, 213302.

(32) Buckley, A.; Pickup, D.; Yates, C.; Zhao, Y.; Lidzey, D. *J. Appl. Phys.* **2011**, *109*, 084509.

(33) Wang, P.-S.; Wu, I.-W.; Tseng, W.-H.; Cheng, M.-H.; Wu, C.-I. *Appl. Phys. Lett.* **2011**, *98*, 173302.

(34) Sun, Y.; Takacs, C. J.; Cowan, S. R.; Seo, J. H.; Gong, X.; Roy, A.; Heeger. *Adv. Mater.* **2011**, *23*, 2226.

(35) Sun, Y.; Welch, G. C.; Leong, W. L.; Takacs, C. G.; Bazan, G. C.; Heeger, A. J. *Nat. Mater.* **2012**, *11*, 44−48.

(36) Chiam, S. Y.; Dasgupta, B.; Soler, D.; Leung, M. Y.; Liu, H.; Ooi, Z. E.; Wong, L. M.; Jiang, C. Y.; Chang, K. L.; Zhang, J. *Sol. Energy Mater. Sol. Cells* **2012**, *99*, 197.

(37) Braun, S.; Salaneck, W. R.; Fahlman, M. *Adv. Mater.* **2009**, *21*, 1450.

(38) Greiner, M. T.; Helander, M. G.; Tang, W.-M.; Wang, Z.-B.; Qiu, J.; Lu, Z.-H *Nat. Mater.* **2012**, *11*, 76.

(39) Greiner, M. T.; Chai, L.; Helander, M. G.; Tang., W.-M.; Lu, Z.-H. *Adv. Funct. Mater.* **2012**, DOI: 10.1002/adfm.201200615.

(40) Vasilopoulou, M.; Palilis, L. C.; Georgiadou, D. G.; Argitis, P.; Kennou, S.; Syggelou, L.; Kostis, I.; Papadimitropoulos, G.; Konofaos, N.; Iliadis, A.; Davazoglou, D. *Appl. Phys. Lett.* **2011**, *98*, 123301.

(41) Vasilopoulou, M.; Palilis, L. C.; Georgiadou, D. G.; Douvas, A. M.; Argitis, P.; Kennou, S.; Syggelou, L.; Papadimitropoulos, G.; Kostis, I; Stathopoulos, N. A.; Davazoglou, D. *Adv. Funct. Mater.* **2011**, *21*, 1489.

(42) Vasilopoulou, M.; Papadimitropoulos, G.; Palilis, L. C.; Georgiadou, D. G.; Argitis, P.; Kennou, S.; Kostis, I.; Vourdas, N.; Stathopoulos, N. A.; Davazoglou, D. *Org. Electron.* **2012**, *13*, 796.

(43) Vasilopoulou, M.; Palilis, L. C.; Georgiadou, D. G.; Kennou, S.; Kostis, I.; Davazoglou, D.; Argitis, P. *Appl. Phys. Lett.* **2012**, *100*, 013311.

(44) Janotti, A; Van de Walle, C. G. *Nat. Mater.* **2007**, *6*, 44.

(45) Van de Walle, C. G.; Neugebauer, J. *Nature* **2003**, *423*, 626−628.

(46) Wei, J.; Ji, H.; Guo, W.; Nevidomskyy, A. H.; Natelson, D. *Nat. Nanotechnol.* **2012**, *7*, 357.

(47) Xu, X.; Randorn, C.; Efstathiou, P.; Irvine, J. T. S. *Nat. Mater.* **2012**, *11*, 595.

(48) Roy, S. C.; Varghese, O. K.; Paulose, M.; Grimes, C. A. *ACS Nano* **2010**, *4*, 1259.

(49) Papadimitropoulos, G.; Vourdas, N.; Giannakopoulos, K.; Vasilopoulou, M.; Davazoglou, D. *J. Appl. Phys.* **2011**, *109*, 103527.

(50) Vourdas, N.; Papadimitropoulos, G.; Kostis, I.; Vasilopoulou, M.; Davazoglou, D. *Thin Solid Films* **2012**, *520*, 3614.

(51) Kostis, I.; Vourdas, N.; Vasilopoulou, M.; Douvas, A.; Konofaos, N.; Iliadis, A.; Davazoglou D. Unpublished results.

(52) Ou, J. Z.; Campbell, J. L.; Yao, D.; Wlodarski, W.; Kalantar-zadech, K. *J. Phys. Chem. C* **2011**, *115*, 10757.

(53) Seguin, L.; Figlarz, M.; Cavagnat, R.; Lassègues, J.-C. *Spectrochim. Acta A* **1995**, *51*, 1323.

(54) Ajito, K.; Nagahara, L. A.; Tryk, D. A.; Hashimoto, K.; Fujishima. *J. Phys. Chem.* **1995**, *99*, 16383−16388.

(55) Eda, K. *J. Solid State Chem.* **1992**, *98*, 350.

(56) Mestl, G.; Ruiz, P.; Delmon, B.; Knözinger, H. *J. Phys. Chem.* **1994**, *98*, 11269.

(57) Ceylan, V. K.; Sourisseau, C.; Brencic, J. V. *J. Raman Spectrosc.* **1985**, *16*, 128.

(58) Scanlon, D. O.; Watson, G. W.; Payne, D. J.; Atkinson, G. R.; Egdell, R. G.; Law, D. S. L. *J. Phys. Chem.* **2010**, *114*, 4636.

(59) Criinert, W.; Stakheev, A. Y.; Feldhaus, R.; Anders, K.; Shpiro, E. S.; Minachev, K. M. *J. Phys. Chem.* **1991**, *95*, 1323.

(60) Fleisch, T. H.; Mains, G. J. *J. Chem. Phys.* **1982**, *76* (2), 780.

(61) Katrib, A.; Benadda, A.; Sobczak, J. W.; Maire, G. *Appl. Catal., A* **2003**, *242*, 31.

(62) Werfer, F.; Minni, E. *J. Phys. C: Solid State Phys.* **1983**, *16*, 6091.

(63) Tokarz-Sbieraj, R.; Grybos, R.; Witko, M. *Appl. Catal., A* **2011**, *391*, 137.

(64) Goodenough, J. B. *Czech. J. Phys.* **1967**, *B17*, 304.

(65) Goodenough, J. B. *Prog. Solid State Chem.* **1971**, *3*, 490.

(66) Goodenough, J. B. *Phys. Rev.* **1960**, *117*, 1442.

(67) Goodenough, J. B. *J. Appl. Phys.* **1960**, *5*, 359.

(68) Sleight, T. P.; Hare, C. R.; Sleight, A. W. *Mater. Res. Bull.* **1968**, *3*, 437.

(69) Greenblatt, M. *Chem. Rev.* **1988**, *88*, 31.

(70) Fleisch, T. H.; Mains, G. J. *J. Chem. Phys.* **1982**, *76* (2), 780.

(71) Dickens, P. G.; Birtill, J. J. *J. Electr. Mater.* **1978**, *7*, 679.

(72) Dickens, P. G.; Birtill, J. J.; Wright, C. J. *J. Solid State Chem.* **1979**, *28*, 185.

(73) Dickens, P. G.; Crouch-Baker, S.; Weller, M. T. *Solid State Ionics* **1986**, *18/19*, 89.

(74) Chen, L.; Cooper, A. C.; Pez, G. P.; Cheng, H. *J. Phys. Chem. C* **2008**, *112* (6), 1755.

(75) Cheng, H.; Chen, L.; Cooper, a. c.; Sha, X.; Pez, G. P. *Energy Environ. Sci.* **2008**, *1*, 338.

(76) Palilis, L. C.; Vasilopoulou, M.; Georgiadou, D. G.; Argitis, P. *Org. Electron.* **2010**, *11*, 887.

(77) Png, R.-Q.; Chia, P.-J.; Tang, J.-C.; Liu, B.; Sivaramakrishnan, S.; Zhou, M.; Khong, S.-H.; Chan, H. S. O.; Buroughess, J. H.; Chua, L.-L.; Friend, R. H.; Ho, P. K. H. *Nat. Mater.* **2010**, *9*, 152.

(78) Fang, J.; Wallikewitz, B. H.; Gao, F.; Tu, G.; Müller, C.; Pace, G.; Friend, R. H.; Huck, W. T. S. *J. Am. Chem. Soc.* **2011**, *133* (683), 68.

(79) Tress, W.; Leo, K.; Riede, M. *Adv. Funct. Mater.* **2011**, *21*, 2140.

(80) Wong, K. H.; Ananthanarayanan, k.; Luther, J.; Balaya, P. *J. Phys. Chem. C2012* **2012**, *116*, 16346.